A Survey of Current Operations-Ready Thermospheric Density Models for Drag Modeling in LEO Operations

Tobiska, W. Kent ; Pilinski, Marcin; Bruinsma, Sean L.; Sutton, Eric ; Knipp, Delores ; Mallik, Vishnuu ; Jagatia, Bhavi ; Siegers, Mike ; Siemes, C.; More Authors

Publication date
2023

Document Version
Final published version

Published in
Proceedings of AMOS 2023

A Survey of Current Operations-Ready Thermospheric Density Models for Drag Modeling in LEO Operations

Shaylah Mutschler
Space Environment Technologies (SET)
W. Kent Tobiska[a], Marcin Pilinski[b], Sean Bruinsma[c], Eric Sutton[d], Delores Knipp[e], Vishnuu Mallik[f], Bhavi Jagatia[f], Mike Siegers[f], Tzu-Wei Fang[g], Tim Fuller-Rowell[h], Brandon DiLorenzo[a], Steve Casali[i], Christian Siemes[j], Kaiya Wahl[a]
[a] *Space Environment Technologies (SET), Pacific Palisades, CA, USA*
[b] *Laboratory for Atmospheric and Space Physics (LASP), University of Colorado at Boulder, Boulder, CO, USA*
[c] *Space Geodesy Office, Centre National d'Etudes Spatiales (CNES), Toulouse, France (CNES)*
[d] *Space Weather Technology, Research and Education Center (SWx TREC), University of Colorado at Boulder, Boulder, CO, USA*
[e] *Smead Aerospace Engineering Science Department, University of Colorado, Boulder, CO, USA*
[f] *Planet Labs PBC, San Francisco, CA, USA*
[g] *National Oceanic & Atmospheric Administration (NOAA), Boulder, CO, USA*
[h] *Cooperative Institute for Research in Environmental Sciences (CIRES) at the University of Colorado Boulder, Boulder, CO, USA*
[i] *Omitron, Beltsville, MD, USA*
[j] *Delft University of Technology, Delft, Netherlands*

ABSTRACT

In Low Earth Orbit (LEO), atmospheric drag is the largest contributor to trajectory prediction error. The current thermospheric density model used by the Combined Space Operations Center (CSpOC) in operations is the High Accuracy Satellite Drag Model (HASDM). Since HASDM is not available for use outside of the US Government, satellite operators are left to determine what publicly available, open-source density model they should integrate into their internal operational software. This decision is nontrivial due to the number of available density models, each having variable performance dependent on several factors including space weather conditions and orbit altitude. To compound matters, the rapid rise of this solar cycle suggests that the predicted solar maximum between 2024-2027 could be higher than the previous solar maximum, thus causing larger perturbations due to drag from atmospheric density on LEO satellites. Given the evermore challenging nature of operations in LEO, it is imperative for satellite operators to update legacy density models to a state-of-the-art density model to provide improved trajectory predictions for collision risk assessment and vital day-to-day operational decisions.

This paper outlines several operations-ready thermospheric density models, describing their performance, computation time, required operational space weather input parameters, and notes for implementation. We define an operations-ready density model as a model that is well-documented, has verified and quantified model performance, and provides publicly available model code for implementation on a user's own system. Operations-ready models include the Drag Temperature Model (DTM), the Jacchia-Bowman 2008 (JB2008) model, the US Naval Research Laboratory Mass Spectrometer and Incoherent Scatter radar 2.0 (NRLMSIS 2.0) model, and the Thermosphere–Ionosphere–Electrodynamics General Circulation Model (TIE-GCM). US Government operational density models, HASDM and the Whole Atmosphere Model and Ionosphere Plasmasphere Electrodynamics (WAM-IPE) model, are included for comparison in the Analysis section. Models are evaluated against *global* HASDM density and *local* Gravity Recovery And Climate Experiment Follow-On (GRACE-FO) satellite accelerometer density data. A propagation analysis is also included in which model performance is compared during quiet and storm conditions and resulting LEO object trajectory prediction errors are quantified at various orbit altitudes. The analysis shows that any of the named operations-ready density models (DTM2020, JB2008, NRLMSIS 2.0, TIE-GCM) are a viable option for satellite operations. In addition to LEO satellite operators, the results from this paper are also informative for the transition of civilian space traffic coordination efforts out of CSpOC and into the Department of Commerce.

1. INTRODUCTION

The Low Earth Orbit (LEO) regime is becoming more congested as the number of satellites continues to grow with the rising popularity and establishment of SmallSat constellations. For example, SpaceX is in the process of creating a 12,000-satellite Starlink constellation in LEO, with more than 4,000 SmallSats in orbit currently. The growth in the number of LEO objects directly increases the probability of unintentional collisions between objects due to accumulating space debris. This could lead to the runaway Kessler syndrome, where unavoidable cascading collisions occur, leading to a potentially unusable LEO orbital domain. In addition to a congested LEO space environment, the rapid rise of this solar cycle suggests that the predicted solar maximum between 2024-2027 could be higher than the previous solar maximum, thus causing higher perturbations due to drag from atmospheric density on LEO satellites. Given the evermore challenging nature of operations in LEO, it is imperative for satellite operators to update legacy density models to reduce density prediction errors and provide improved trajectory predictions for collision risk assessment and vital day-to-day operational decisions.

The Combined Space Operations Center (CSpOC) is responsible for the detection, identification, and daily tracking of all human-made objects in space. CSpOC also provides a conjunction analysis service that alerts satellite operators if their satellite exceeds a specific collision probability threshold with another Resident Space Object (RSO). The current thermospheric density model used by CSpOC in operations, the High Accuracy Satellite Drag Model (HASDM) [77], applies corrections to an empirical density model every 3 hours using observations of 80+ calibration satellites. Since HASDM is not available for use outside of the US Government, satellite operators are left to determine which publicly available, open-source density model they should integrate into their internal operational software. This decision is nontrivial due to the number of available density models, each having variable performance dependent on several factors including space weather conditions and orbit altitude [12], [66].

This paper outlines several operations-ready thermospheric density models, describing their performance, computation time, required operational space weather input parameters, and notes for implementation. We define an operations-ready density model as a model that is well-documented, has verified and quantified model performance, and provides publicly available model code for implementation on a user's own system. An operations-ready density model must also be able to run in near real-time such that the processing speed is faster than the wall clock using reasonable computational hardware. The models that meet these criteria are the Drag Temperature Model (DTM), the Jacchia-Bowman 2008 (JB2008) model, the US Naval Research Laboratory Mass Spectrometer and Incoherent Scatter radar 2.0 (NRLMSIS 2.0, shortened to MSIS2.0) model, and the Thermosphere–Ionosphere–Electrodynamics General Circulation Model (TIE-GCM). US Government operational density models, HASDM and the Whole Atmosphere Model and Ionosphere Plasmasphere Electrodynamics (WAM-IPE), are included for comparison in the Analysis section. WAM-IPE is run operationally at National Oceanic and Atmospheric Administration (NOAA) and was recently designated as one of the density models in the Department of Commerce's (DoC) new Space Traffic Management (STM) system in development. All models included in this paper are at a Technology Readiness Level (TRL) of eight or nine, meaning that they have validated performance under operational conditions or they are currently run on an operational system.

This paper is organized as follows. Section 2 provides an overview of space weather, with subsections on the mechanisms that drive variations in thermospheric density, how we quantify space weather activity to drive density models, and an overview of thermospheric density. A description of satellite drag and its calculation is provided in Section 3. Section 4 reviews the various operations-ready and US government operational thermospheric density models. In Section 5 we analyze the performance of the operations-ready density models, comparing them to each other, the Gravity Recovery And Climate Experiment Follow-On (GRACE-FO) accelerometer-derived density, HASDM, and WAM-IPE. We conclude with a summary of our findings.

This paper is not meant to be a comprehensive evaluation of each density model, but rather an overview of the density modeling options available to LEO operators. The information provided is intended to assist satellite operators with updating their density models to meet the performance needs of an increasingly congested LEO environment and the fast-approaching solar maximum.

2. SPACE WEATHER

Drag is the largest contributor to LEO trajectory prediction error and is determined primarily by thermospheric density. This section provides the background information necessary to understand thermospheric density and the space

weather that drives its dynamic nature. A description of the operational space weather measurements used to drive density models is also provided.

2.1 Sun-Earth Interaction

Disturbances in the near-Earth space environment are driven by the Sun and its interactions with geospace. The primary energy input into the thermosphere is solar irradiance in the form of soft X-ray Ultra-Violet (XUV, 1-30 nm), Extreme Ultra-Violet (EUV, 30-120 nm), Lyman-α (121 nm), and Far Ultra-Violet (FUV, 122-200 nm) [31]. Variations in XUV, EUV, Lyman-α, and FUV solar irradiance drives variations in the overall heating of the thermosphere on a slower time scale than geomagnetic activity.

The second most important energy input to the thermosphere is geomagnetic activity caused by the interaction between the solar wind and the Earth's magnetic field. More specifically, Coronal Mass Ejections (CME) and high-speed solar wind cause disturbances in the Earth's magnetic field that lead to thermospheric density enhancements. CMEs are magnetized plasma bubbles that erupt from the Sun and travel outward through the interplanetary medium. Depending on the origin and direction of travel, some CMEs collide with Earth's magnetic field and cause weak to strong geomagnetic storms depending on their polarity. Solar wind is an ongoing outflow of the Sun's coronal plasma into the interplanetary medium. High-Speed Streams (HSS) emanate from open magnetic field regions in the Sun's corona. Interactions between slow and fast solar wind cause Co-rotating Interaction Regions (CIR). When solar wind HSS and/or CIR interact with Earth, the field irregularities in the plasma may contribute to moderate geomagnetic storms. Both CMEs and high-speed solar wind can cause geomagnetic storms, which lead to thermospheric density enhancements. Knipp [32] provides a comprehensive text on these topics.

The frequency and magnitude of thermospheric density enhancements stemming from solar short-wave irradiance (XUV, EUV, Lyman-α, and FUV) variations and geomagnetic activity are dependent on the approximately 11-year solar cycle and 27-day solar rotation. During an 11-year solar cycle, the Sun experiences a solar minimum and maximum in the number of sunspots and active regions. We are currently experiencing the rise of solar cycle 25. The Sun's short-wave irradiance increases as it approaches solar maximum because active regions of the Sun (i.e., magnetically induced enhancements to the solar atmosphere above sunspots) produce the largest quantity of solar flux. Similarly, the frequency and magnitude of CMEs and solar flares peak during solar maximum or shortly thereafter. Fig. 1 shows solar radio flux emission at 10.7 cm for solar cycles 24 and 25. The solar short-wavelength flux, represented by F10.7 proxy, is currently higher than what was predicted for this cycle, which strongly suggests that the upcoming solar maximum will be higher than the previous one.

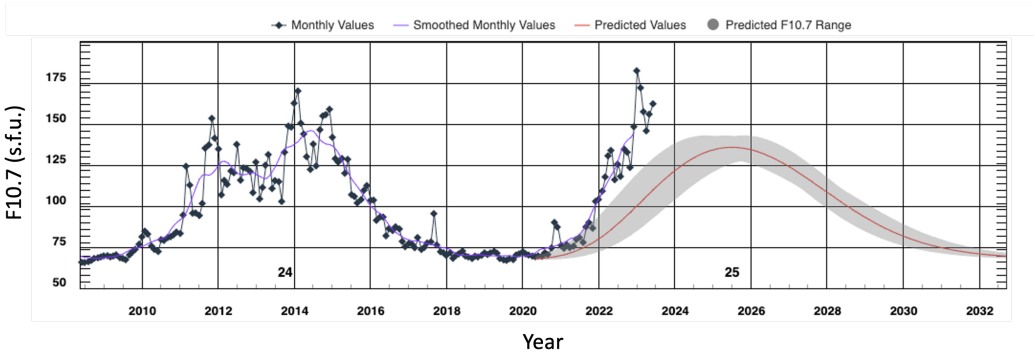

Fig. 1. Solar Cycle F10.7cm Radio Flux Progression
Credit: NOAA SWPC [58]

2.2 Solar and Geomagnetic Model Drivers

Solar and geomagnetic drivers play a crucial role as inputs in thermospheric density models. Kp, Ap, and F10.7 are commonly used legacy model drivers; additional, more contemporary drivers include Dst, S10, M10, Y10 and F30. This section provides a description of the operational solar and geomagnetic drivers utilized as inputs for thermospheric density models. A more comprehensive description of drivers can be found in the ISO International Standard on Earth upper atmosphere [29].

It is important to recognize a fundamental distinction of thermospheric density model drivers: they are categorized as either proxies, indices, or both. A solar irradiance proxy is a measurement of the solar flux at a particular wavelength,

but is used as a proxy for another wavelength because of its high correlation to the other wavelength. An example of this is F10.7, which serves as a proxy for solar EUV emissions. F10.7 is an EUV proxy because it measures the solar radio flux at 10.7-cm wavelength (radio spectrum), which is not absorbed by the atmosphere and therefore has no direct impact on thermospheric density and can be measured from the ground regardless of terrestrial weather conditions. F10.7 is a very reliable and well-calibrated radio flux index, which is still the most used despite the availability of EUV measurements from space. Since 2013, the F30 proxy (solar radio flux at 30 cm), which mimics the EUV irradiance better than F10.7, has been used in some DTM versions. The M10 proxy is derived from the Mg II core-to-wing ratio [95] and is measured from the Geostationary Operational Environmental Satellite (GOES) series satellites via Extreme Ultraviolet and X-ray Sensors (EXIS)/Extreme Ultraviolet Spectrometer (EUVS). M10 indicates the heating of O_2 occurring in Earth's atmosphere at 100-110 km altitude by photons originating from the solar chromosphere and photosphere in the Schumann-Runge Continuum near 160 nm [90].

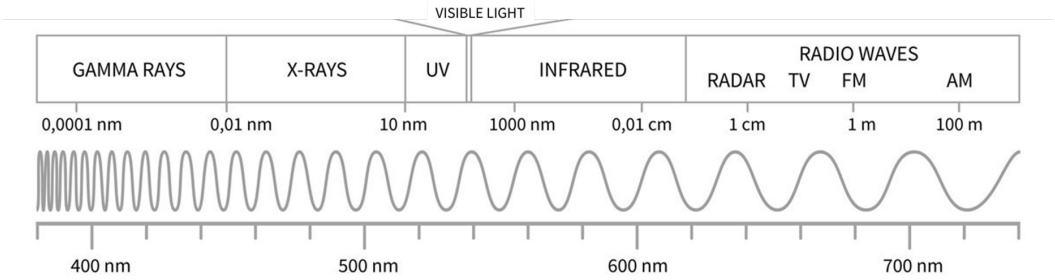

Fig. 2. Solar irradiance wavelength spectrum. The visible portion of the spectrum is expanded at the bottom.

Thermospheric heating is predominantly driven by solar chromospheric EUV energy, complemented by contributions from coronal soft X-ray, Lyman-α, and photospheric FUV wavelengths [89]. A range of solar irradiances in a variety of wavelengths emanate from the Sun. Upon reaching Earth, the Sun's photons are absorbed by distinct atomic and molecular species, each at specific unit optical depth layers in the atmosphere [89]. It is with this understanding that Tobiska developed the M10, S10, and Y10 *indices* [90] for utilization in the JB2008 model.

Each of these indices indicates the amount of solar flux energy being transferred to a particular altitude range of the Earth's atmosphere. The S10 and Y10 indices are measurements of solar short-wave irradiance, which are absorbed by the atmosphere and therefore directly affect thermospheric density. The S10 index is the integrated 26–34 nm solar irradiance (EUV) that was originally measured by the Solar Extreme-ultraviolet Monitor (SEM) instrument on a number of satellites including the NASA/European Space Agency (ESA) Solar and Heliospheric Observatory (SOHO) research satellite (Lagrange Point 1 (L1) on the Earth-Sun line) [9] and is now operationally observed by the GOES series satellites. S10 represents the heating of atomic Oxygen occurring above 200 km altitude in Earth's atmosphere by photons originating from the solar chromosphere. The Y10 index is a combination of 0.1–0.8 nm X-rays and 121 nm Lyman-α; it is weighted to represent mostly X-rays during solar maximum and mostly Lyman-α during moderate and low solar activity [9]. Measurements for the Y10 index are collected via the X-ray spectrometer (XRS) and EXIS instruments on NOAA GOES satellites. Y10 represents the heating of N_2, O_2, H_2O, nitric oxide (NO) occurring in Earth's atmosphere at 85-90 km altitude by photons originating from the solar transition region and corona. F10.7, M10, S10, and Y10 are all daily indices and are provided in solar flux units (s.f.u.).

The Kp/Ap, and Dst indices describe geomagnetic activity. They are proxies for upper atmosphere heating due to interaction with the solar wind. Kp/Ap characterizes the intensity of the geomagnetic field disturbance derived from 13 magnetometers distributed across mid-latitudes worldwide [25]. The Ap index is the linear form of the quasi-logarithmic Kp index; a mapping between the two indices is provided by NOAA [54]. Kp ranges from 0 to 9 (dimensionless), while Ap ranges from 0 to 400 (nT). Both have a time resolution of three hours. Dst is an indicator of the strength of the storm-time ring current in the inner magnetosphere and is calculated hourly using measurements from four off-equatorial magnetic observatories [78], [97]. During the main phase of geomagnetic storms, the ring current becomes highly energized and produces a southward-directed magnetic field perturbation at low latitudes on the Earth's surface [9]. This is opposite to the normal northward-directed main field. Dst has a time resolution of one hour, which provides a finer assessment temporally of the evolution of geomagnetic storms compared to Ap or Kp. Fig. 3 provides plots of the Kp, Dst, F10, M10, S10, and Y10 drivers during the month of April 2023.

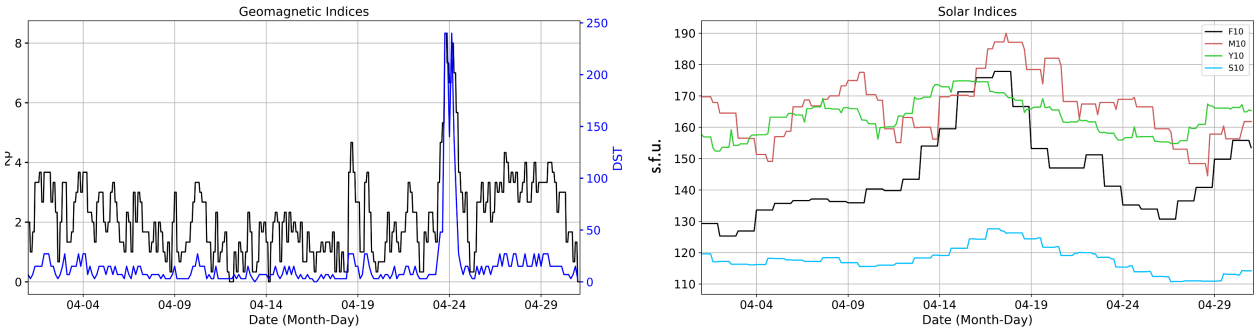

Fig. 3. April 2023 solar and geomagnetic drivers

Improved thermospheric density forecasts are a critical need identified by the Space Weather Operations, Research, and Mitigation (SWORM) Working Group, a Federal interagency coordinating body [52]. Errors in thermospheric density predictions are a function of both the density model and the model drivers and their predictions. The error caused by each is about the same order of magnitude. This paper primarily explores performance based on density model rather than model drivers and their predictions. Although several sources provide forecast drivers, the accuracy of these forecasts vary depending on several factors. In a recent study benchmarking forecast drivers and their success, Licata, et al. [37] found that the performance of forecast JB2008 indices degrades during periods of high activity levels, where the Sun is more volatile. They concluded that flaring active region evolution is still poorly predicted, affecting the S10 index, while the magnitude and timing for the Dst index is also not well predicted.

Space Environment Technologies (SET) is currently working on updates to the nowcast S10 and the forecast S10 and Dst inputs to JB2008 and HASDM. The improved nowcast S10 and forecast S10 and Dst are expected to be available operationally in early 2024 and 2025, respectively. It is expected that an improvement to these indices will lead to improved JB2008 and HASDM performance.

The various solar and geomagnetic drivers that are required for each operations-ready density model are provided in Table 1. Operational solar and geomagnetic drivers are available from a number of sources. The GFZ German Research Centre for Geosciences provides Kp, Ap, and F10.7 nowcasts [26]. NOAA Space Weather Prediction Center (SWPC) provides a 3-day Kp forecast with a 3-hour time resolution [55], as well as 45-day Kp and F10.7 forecasts with a one-day time resolution [56]. Celestrack provides Kp and F10.7 nowcasts, three-day Kp forecasts (at a 3-hour time resolution), and a 45-day forecast of the daily Kp and F10.7 [15]. The forecast drivers provided by Celestrack are the same as those provided by NOAA SWPC. The quick-look Dst index is released through the World Data Center in Kyoto, Japan [99]. Collecte Localisation Satellites (CLS) provides the F30 nowcast and 30-day forecasts [16]. SET provides operational F10.7, M10, S10, Y10, Ap, and Dst indices, updated hourly, via a subscription service on the U.S. Space Force Unified Data Library (UDL). The SET UDL subscription service includes nowcasts and a 6-day forecast of all indices.

Table 1. Required Space Weather Drivers for each Operations-Ready Density Model

Model / Driver	**Kp/Ap**	**Dst**	**F10.7**	**S10, M10, Y10**
DTM2020	X		X	
MSIS2.0	X		X	
JB2008	X	X	X	X
TIE-GCM	X		X	

2.3 Thermospheric Density

Thermospheric density is highly dynamic and its variability depends on a number of factors, including solar activity, geomagnetic activity, diurnal cycle, season, altitude, and latitude. Most of these factors are directly linked to the Sun. Solar cycle and solar activity describe the Sun's short-wave irradiance, and geomagnetic activity is a measure of disturbance in the Earth's magnetic field caused by solar wind (i.e., particles) and interplanetary magnetic field (IMF). The Sun-Earth geometry leads to a seasonal, diurnal, and semidiurnal cycle. Thermospheric density decreases

exponentially as a function of altitude, and therefore affects the trajectories of LEO objects more than higher orbital regimes.

Periods of time when there is little to no geomagnetic field disturbance and relatively low solar flux are referred to as quiet conditions; whereas storm-time refers to periods of time when there is a major disturbance in the near-Earth space environment caused by a geomagnetic storm or solar activity. Density is typically highest around 2-4pm local time, and lowest from 2-5am local time and in the polar region experiencing winter.

3. SATELLITE DRAG

An object in LEO experiences atmospheric drag caused by particles in the atmosphere colliding with the surface of the object. In fact, atmospheric drag is the second largest perturbation on LEO object motion; with J2 gravity effects caused by the non-sphericity of the Earth being the largest perturbation. Drag acts primarily in the opposite direction of the object's velocity vector and effectively dissipates orbit energy. A simplifying assumption of aerodynamic symmetry is often made that results in the drag force that is directed opposite the relative velocity. The magnitude of the force due to drag is directly dependent on neutral density. This is generally modeled as follows:

$$a_{drag} = -\frac{1}{2}\rho\frac{C_D A}{m}v_{rel}^2\frac{\vec{v}_{rel}}{|\vec{v}_{rel}|} \quad (1)$$

where

$$\vec{v}_{rel} = \frac{d\vec{r}}{dt} - \vec{\omega}_{\oplus} \times \vec{r} \quad (2)$$

is the velocity vector relative to an atmosphere co-rotating along with the Earth; C_D is the drag coefficient; A is the exposed cross-sectional area to the particle flow (area projected onto a plane normal to $\vec{v}_{rel}$); m is the object's mass; $\vec{\omega}_{\oplus}$ is the mean motion of the Earth's rotation; $\vec{r}$ is the object position vector in an Earth Centered Inertial reference frame; and ρ is thermospheric density [93]. The drag coefficient, mass, and area of the object are typically combined to form the ballistic coefficient ($\beta = C_D A/m$). C_D and A can vary in time as a function of spacecraft attitude. The cross-sectional area A is computed using a spacecraft geometry model (sometimes referred to as a macro model) and attitude information. There are two options for obtaining the C_D of a satellite, 1) estimate C_D by fitting observations of the drag and the chosen density model, 2) compute the physical C_D. Estimating C_D inherently de-biases the density model and is a popular choice in space operations. The physical C_D is a function of ambient conditions such as atmospheric gas temperature, velocity, and composition. There is presently no consensus on which C_D model is best, but the more realistic ones require the individual species densities, which can be provided by models such as MSIS or DTM. An example of a physical C_D model is posted here [85]. More information on C_D can be found in the following publications [4], [5], [44], [46], [71], [63], [40], [41].

4. THERMOSPHERIC DENSITY MODELS

Current methods that model thermospheric density can be categorized as empirical or physics-based. Empirical models use both short and long-term trends from measurements using multiple instruments to provide a parameterized mathematical formulation of the system. Physics-based models represent the underlying dynamics of the system, but require substantially more computing resources than empirical models [45]. Although empirical models have historically been applied in operations due to their faster and more efficient nature, as computation power becomes more accessible, the incorporation of physics-based models, like the TIE-GCM is becoming tractable in operations.

Another type of density modeling is data assimilative, where direct or indirect density measurements are assimilated to apply corrections to an empirical or physics-based background density model. HASDM is an example of a data assimilative density model that uses an empirical background model, JB2008, and assimilates indirect measurements of density in the form of satellite arcs [7], [8], [77]. Current research efforts are exploring data assimilation with both empirical and physics-based models. For example, Dragster assimilates orbital observations to estimate drivers of empirical density models [64], and the Iterative Driver Estimation and Assimilation (IDEA) assimilates high-cadence accelerometer data to estimate drivers of a physics-based density model [82]. Nevertheless, other than HASDM, none of the data assimilation density models are ready for operations at this time.

4.1 Operations-Ready Density Models

This section provides an overview of the operations-ready density models. These are models that are well-documented, model performance has been verified and quantified, and the model code is publicly available for implementation on a user's system. For each model, we provide information such as model inputs/outputs, where to obtain the model and required inputs, general model performance, and model limitations/degradations.

4.1.1 DTM

The first Drag Temperature Model, DTM78 [2], was developed in the seventies. The latest release is DTM2020 [13]. DTM2020 is considered an empirical model. It was constructed by optimally fitting model coefficients to the complete CHAllenging Mini satellite Payload (CHAMP) [20], GRACE [11] and Gravity field and steady-state Ocean Circulation Explorer (GOCE) [10] high-resolution accelerometer-inferred density datasets, as well as Swarm A densities [94], Stella daily-mean densities [11], and daily-mean global average mass densities at 250 and 325 km altitude derived from two-line orbital element sets (TLE) [22]. A major difference between the operational version of DTM2020 and DTM2013 concerns the drivers, which are F10.7 and Kp and F30 and Kp, respectively. Secondly, the density datasets were not adjusted to the U.S. Space Force HASDM model [77] by means of scaling factors, as described for GOCE data in [10]. Instead, CHAMP, GOCE, and Swarm A densities were considered of higher absolute accuracy and used unmodified. Consequently, DTM2020 densities are on average 20-30% smaller than DTM2013 and HASDM. Smaller absolute densities are consistent with MSIS2.0 [21], which also predicts smaller densities than NRLMSISE-00 (shortened to MSIS-00). Fig. 4 provides a comparison between DTM2020 and DTM2013 global mean density at 200, 400, and 550 km altitude for the month of April 2023. DTM2020 density is noticeably lower than DTM2013 during both the quiet and storm conditions during this time period.

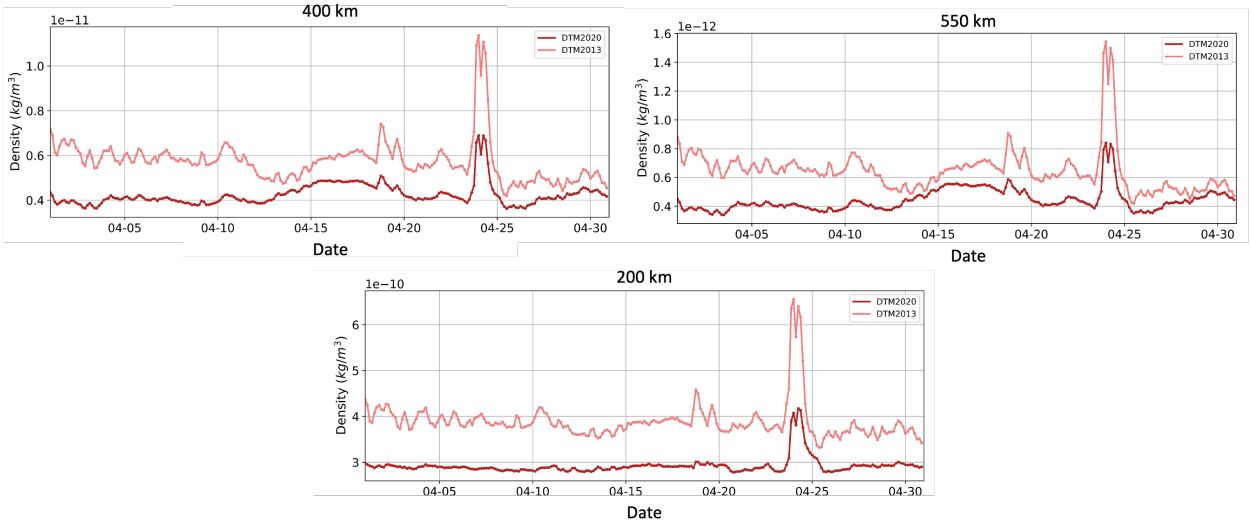

Fig. 4. April 2023 comparison of DTM2020 and DTM2013 global mean density

In DTM2020, total density is calculated via the addition of the partial densities of the main thermosphere constituents (N_2, O_2, O, He, H), under the hypothesis of independent static diffuse equilibrium. Temperatures and density variations as a function of latitude, local solar time, season, solar flux, and geomagnetic activity are modeled by means of a spherical harmonic function. DTM2020 ranges from 120 to 1500 km altitude. Model performance is very good between 180 and 400 km altitude; there is insufficient quality data below 180 km to assess performance. DTM2020 is less precise for high solar activity (81-day mean F10.7 > 180) due to the lack of representation of those conditions in the density datasets used to build the model. DTM2020 overall performance degrades at higher altitudes (>500 km). However, because DTM models constituents, helium modeling is qualitatively correct, notably in the winter helium bulge, which is an increase of the helium concentration in the winter hemisphere of the thermosphere by 1 to 2 orders of magnitude relative to the summer hemisphere.

DTM is currently run at the National Centre for Space Studies (CNES) (all DTM versions), ESA, the United Kingdom (UK) Met Office (DTM2013), and NASA Community Coordinated Modeling Center (CCMC) (DTM 2013 and 2020).

DTM is also integrated into Bernese GNSS software (DTM 2013 and 2020) [3], NASA Jet Propulsion Lab's (JPL) Mission Analysis, Operations, and Navigation Toolkit Environment (MONTE) (DTM 2013 and 2020) [51], NASA JPL's GNSS-Inferred Positioning System (Gipsy-X) (DTM2013) [6], NASA Goddard's GEODYN (DTM 94 and 2013) [50], the Orekit astrodynamics toolkit (DTM2000) [60], and the Orbit Determination Tool Kit (ODTK) (DTM 2013 and 2020) [1]. DTM2020 Fortran code (with Python wrapper option) and documentation is available at [84]. Running on a standard modern laptop, DTM takes seconds to produce one day of global density with a 3-hour time resolution and a spatial resolution of 10-km altitude, 10-deg latitude, and 1-hour local time.

4.1.2 JB2008

JB2008 is an empirical thermospheric density model and serves as the background model of HASDM, the operational thermospheric density model used by the Space Force for STM. It is the most recent model in the line of Jacchia and Jacchia-Bowman models beginning with the Jacchia Reference Atmosphere in 1970 [30]. JB2008 is the recommended model internationally [29] for specifying neutral densities in LEO as they affect satellite drag. Four different density data sources were used in the development of the JB2008 model. These sources included Air Force daily density values from 1997 to 2007, Air Force HASDM densities from 2001 to 2005, CHAMP accelerometer densities from 2001 to 2005, and GRACE accelerometer densities from 2002 to 2005. In addition to F10.7, JB2008 uses solar irradiance indices M10, S10, and Y10 that are derived from solar short-wave irradiance space-based sensor data. It was the ability to insert more physics into thermospheric density drivers (S10, M10, Y10) in the form of specific solar wavelengths linked to optical depths that enabled JB2008 to substantially reduce thermospheric densities' variation uncertainties [9], [39], [90]. The Dst geomagnetic index is used during storm conditions, while the Ap geomagnetic index is applied during quiet to slightly disturbed non-storm conditions. Use of the Dst index during storm conditions instead of the Ap index greatly reduced density errors, especially during major geomagnetic storm periods. The model solves for exospheric temperature and semiannual density corrections to obtain global thermospheric density variations. The JB2008 model was validated through comparisons of accurate daily density drag data previously computed for numerous satellites at altitudes of 200-1100 km, and from precise CHAMP and GRACE satellite accelerometer density data.

JB2008 does not model individual species densities, and therefore experiences performance degradation at altitudes higher than the oxygen-helium transition layer (400-500 km altitude depending on solar activity) where helium becomes the dominant species. This impacts modeling of particular phenomena such as the winter helium bulge. JB2008 also does not capture post-storm cooling, which is where post-storm density decays to lower than pre-storm levels due to overproduction of NO; this is an area of active research in the thermosphere modeling community.

JB2008 is driven by recent, current, and predicted solar and geomagnetic indices provided by SET, including the S10, M10, Y10, and F10 solar indices as well as Dst and Ap geomagnetic indices [90]. Model Fortran code, Python wrapper, and historical model inputs are available at [74]. JB2008 is also included in the Orekit astrodynamics toolkit [61] and MATLAB [43]. Running on a standard modern laptop, JB2008 takes seconds to produce one day of global density with a 3-hour time resolution and spatial resolution of 10-deg latitude, 10-deg longitude, and 10-km ranging 120 to 1500 km altitude.

4.1.3 MSIS

The ISO International Standard 14222 on Earth's upper atmosphere recommends using the MSIS2.0 empirical model for relative constituent abundances. The MSIS series of models provide atmospheric temperature, number densities of eight species, and mass density. MSIS2.0 was recently developed in 2020 as an improvement to MSIS-00. There were several updates implemented to create MSIS2.0, including incorporation of extensive new (post-2000) lower and middle atmosphere temperature, O, and H data, along with global average thermospheric mass density derived from satellite orbits [21]. Additionally, major changes to the model formulation were implemented, including a temperature-dependent connection between densities in the lower/middle atmosphere and the thermosphere [21]. As a result of all the updates, N_2 and O densities (the major constituents below 400 km altitude) in the thermosphere are lower in MSIS2.0 than MSIS-00. Fig. 5 provides a comparison between MSIS2.0 and MSIS-00 global mean density at 200, 400, and 550 km altitude for the month of April 2023. The difference between MSIS2.0 and MSIS-00 is largest, relatively, at 200 km altitude with approximately a 10% difference, and lowest at 550 km altitude with a difference of only a few percentage points.

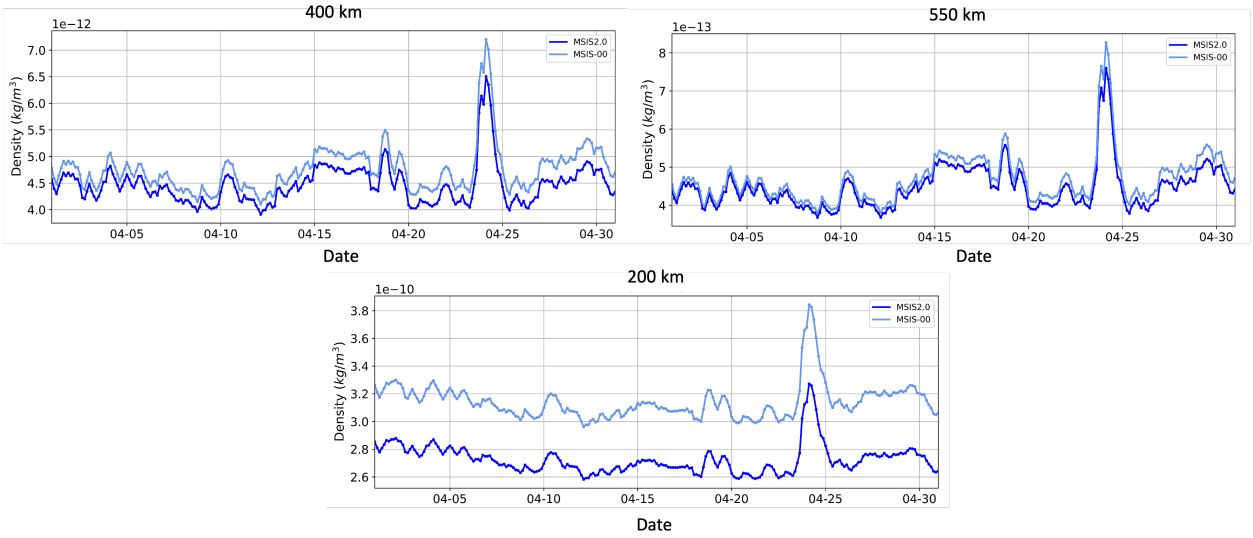

Fig. 5. April 2023 comparison of MSIS2.0 and MSIS-00 global mean density

The MSIS2.0 model generates a density value when provided with local time, altitude, day of year (DOY), F10.7 index, and the Ap index. MSIS2.0 requires a license for operational use. Fortran code and data samples are available at [92]. A python wrapper of MSIS-00 and MSIS2.0 is available at [86]. MSIS-00 is available as part of Orekit [62]. Both MSIS2.0 and MSIS-00 are run at NASA CCMC. A version of MSIS is integrated into several software packages, including NASA JPL's Gipsy-X, NASA Goddard's GEODYN [50], and NASA's General Mission Analysis Tool (GMAT) [49]. Running on a standard modern laptop, MSIS2.0 takes seconds to produce one day of global density with a 3-hour time resolution and spatial resolution of 10-deg latitude, 10-deg longitude, and 10-km ranging 120 to 1500 km altitude.

4.1.4 TIE-GCM

TIE-GCM is a physics-based space weather model developed at the National Center for Atmospheric Research (NCAR) High-Altitude Observatory (HAO) [65]. The original version of the model, the thermosphere general circulation model (TGCM), was developed by Dickinson et al. [17], [18] and Roble et al. [70]. In its current form, TIE-GCM is a global 3D numerical model that simulates the coupled thermosphere-ionosphere system from about 97 to 500-600 km altitude, the latter being dependent on solar activity [81]. For higher altitudes, an extrapolation scheme must be included for each neutral species based on its exospheric scale height. TIE-GCM self-consistently solves the fully coupled, nonlinear, hydrodynamic, thermodynamic, and continuity equations of the neutral gas, the ion and electron energy and momentum equations, the ion continuity equation, and neutral wind dynamo. The standard spatial resolution is a 5-deg by 5-deg horizontal grid although higher resolution runs can be configured. A pressure-based vertical coordinate is used and must be converted to altitude before computing drag. Some dynamic features of the lower and middle atmosphere are ignored, which could lead to uncertainty when estimating corrections to the external forcing.

TIE-GCM can be driven by several methods and data streams but in its default setting is primarily driven by forcing parameters, Kp and F10.7; however, several additional input parameters and model tuning parameters can be provided as model input. More specifically, solar inputs are driven using the F10.7 proxy [65]. Tidal forcing at the lower boundary is specified by the Global Scale Wave Model. While running in standard resolution, semi-annual and annual density periodicities are taken into account by applying seasonal variation of the eddy diffusivity coefficient at the lower boundary [27]. The electrodynamic potential field is internally generated at middle and low latitudes using the model densities and neutral winds. This is merged with a magnetospheric potential at high latitudes, using one of two available empirically driven models: 1) the empirical formulation of the Heelis high-latitude ionospheric convection model, which is driven by the Kp index, and is the standard TIE-GCM input [28], 2) the Weimer empirical model, which uses upstream solar wind and IMF as input [96]. Recent developments to TIE-GCM (TIE-GCM 2.0 released in 2015) include the addition of helium for high-altitude extension and lower boundary options. This is important for representing thermospheric mass density above 400-500km where helium becomes the dominant species. Species densities for O, O_2, N_2, N, NO, and helium (HE) are available as output in TIE-GCM.

Validation was performed via comparison to CHAMP, GRACE and GOCE density data during 13 geomagnetic storms [14]. Model density data from several models (MSIS-00, JB2008, DTM2013, the Coupled Thermosphere Ionosphere Plasmasphere Electrodynamics Model (CTIPe), and TIE-GCM) were compared to the in-situ satellite density measurements and it was found that TIE-GCM and DTM2013 had the best performance [14]. More thorough model assessment is still required to evaluate dependencies on solar cycle, local time, and altitude effects under storm conditions.

Similar to MSIS2.0, TIE-GCM 2.0 requires a license for operational use; earlier versions of TIE-GCM due not have this restriction. Model code and documentation is available at [53]. TIE-GCM is also available to run via Docker [87], provided by Space Weather Technology, Research and Education Center (SWx TREC) at the University of Colorado Boulder (CUB). TIE-GCM is run at NASA CCMC. Running on a standard modern laptop, TIE-GCM takes less than ten minutes to produce one day of global density with a 1-hour time resolution and spatial resolution of 5-deg latitude, 5-deg longitude, and vertical pressure level size of a half-scale height ranging from approximately 100 to 600 km altitude.

4.2 US Government Operational Density Models

This section provides a description of two US Government operational density models, HASDM and WAM-IPE. These models are included for comparison in the Analysis section.

4.2.1 US Space Force HASDM

HASDM is the operational density model used by the US Space Force CSpOC. It assimilates ground-based radar measurements of 80+ calibration satellites to solve for temperature corrections, calibrating the JB2008 density model and producing a global thermospheric density solution [7], [8], [77]. Intensive sensor tasking is made available for this effort, which allows for the collection of approximately 500 observations per day per calibration satellite. The adjusted atmosphere is forecast beyond the current epoch using JB2008 forecast indices out to 144 hours (6 days) for STM. In 2020, a 20-year HASDM density database spanning 2000 to 2019 was released to the public by Space Environment Technologies [91]. HASDM and its operational densities are not available outside of the Space Force. Historical HASDM operational densities are available via the SET HASDM density database.

The publicly-available SET HASDM nowcast density database [91] currently ranges 2000 to 2019 [73]. The April 2023 HASDM density data used for the Analysis section is not yet available in the SET HASDM density database, but there are efforts to expand the SET HASDM density database through to more recent time periods. There is a community-wide need to establish a density forecast benchmark, so there are also efforts to create a publicly-available SET HASDM density *forecast* database.

4.2.2 NOAA SWPC WAM-IPE

Although the WAM-IPE model is not available for implementation on a system outside of NOAA, we think it is important to include in this paper because 1) the DoC is likely to utilize WAM-IPE as one of its thermospheric density models in their new STM system, and 2) WAM-IPE's global thermospheric density nowcast and forecast outputs are available operationally for integration into astrodynamics toolkits. Unlike HASDM, WAM-IPE does not currently employ data assimilation to correct the thermosphere; the current data assimilation scheme in WAM-IPE is only applied below 60 km altitude. It is important to note that WAM-IPE has not yet been validated to determine if it has attained the level of accuracy required for STM operations. SWPC continues to improve the WAM-IPE model with plans to work with the larger space weather enterprise to incorporate data from satellites used in the COSMIC-2 and GOLD missions as well as other commercial satellite providers. This includes development of data assimilation schemes for the Ionosphere-Thermosphere region.

WAM-IPE is a physics-based model developed by NOAA and University of Colorado researchers to provide operational specification of the ionosphere, thermosphere, and lower atmosphere conditions. The model predicts how Earth's upper atmosphere will respond to solar and geomagnetic conditions as well as the perturbations from the lower atmosphere. WAM-IPE is itself a coupled model consisting of two components, WAM and IPE. The WAM is a General Circulation Model (GCM) extending from the Earth's surface to about 600 km altitude under average solar activity conditions; while the IPE (ionosphere-plasmasphere-electrodynamics) model provides the plasma component of the atmosphere, extending from 90 km to approximately 10,000 km [42], [79]. WAM treats major species O, O_2, and N_2 self-consistently, including large-scale transport, simple oxygen chemistry, and mutual diffusion both in the vertical and horizontal. The WAM lower atmosphere sources include thermospheric tides in lower thermosphere

dynamo region, changes in stratospheric circulation, molecular and atomic atmospheric composition, and composition variability. These mechanisms are coupled to IPE to enable the plasma to respond to changes driven by the neutral atmosphere [69], [67]. WAM has a resolution of 1.89 deg. in latitude and longitude (94x192) with 150 vertical levels ranging from the ground to 600 km altitude. The neutral density has been extended to 1000 km by incorporating MSIS helium above the WAM upper boundary. WAM-IPE uses an arithmetic mean of daily F10.7 and an 81-day average to feed a combination of the solar EUV irradiance model for aeronomic calculations (EUVAC) and high-resolution EUVAC (HEUVAC) models [68], while the solar wind-magnetospheric driving of the high-latitude electric field is calculated by the Weimer empirical model [96].

WAM-IPE has been operational at NOAA since July 2021 and is run every 6 hours in two-day forecast mode using the WAM Data Analysis System (WDAS). The official WAM-IPE operational nowcast output that has been archived from July 2021 to July 2022, as well as the ongoing operational output data stream that began in March 2023; both are available through the SWPC-CCMC joint collaboration [48]. In addition to this nowcast archive, SWPC has recently established a routinely updated operational archive making the full two-day forecast output available [59]. This archive begins on 21 March 2023 and continues to the present time, with continuous updates as the operational runs become available.

5. ANALYSIS

This section provides various analyses comparing the operations-ready density models to each other, to HASDM, and to GRACE-FO accelerometer-derived density. For the purpose of this paper, only the most recent versions of the operations-ready density models are analyzed (i.e., DTM2020, JB2008, MSIS2.0, TIE-GCM 2.0). Because true global density is not available, operations-ready models are compared to HASDM density for global performance evaluation and the propagation analysis. April 2023 is the chosen time period for this study because WAM-IPE operational densities became available in March 2023, and this time period includes both calm and storm conditions. Plots directly comparing HASDM and WAM-IPE are presented for the first time, as HASDM density data post-2020 are not yet publicly available.

This section is not meant to be a comprehensive evaluation of each density model, but rather an example of model performance during quiet and storm geomagnetic conditions and moderate solar irradiance. One month of model assessment is not sufficient to determine overall model performance. Model biases fluctuate between time periods for a variety of reasons; a certain model that performs well during this particular time period of April 2023, may not perform well a month later, during another season, during another geomagnetic activity level, or during a different phase of the solar cycle.

5.1 Global Mean Density

Fig. 6 shows the April 2023 global mean density time-series of each model at altitude shells of 200, 400, and 550 km in the bottom, middle, and top plot, respectively. Overall, the density is relatively low during quiet conditions, before April 24th and after April 25th, and peaks during the geomagnetic storm on April 24th. In addition to the peak from the geomagnetic storm, there is a smaller density enhancement that occurs April 14-20 caused by an increase in solar irradiance (as shown in Fig. 3 by F10.7, S10, M10, and Y10). JB2008, HASDM, and WAM-IPE densities include more high frequency signals at approximately 10-20% amplitude levels which are largely absent in DTM, MSIS2.0, and TIE-GCM; at 200 km altitude all models except for TIE-GCM display this higher frequency (3-6 hour) variability although it is still most pronounced in JB2008 and HASDM. WAM-IPE global mean density is noticeably higher than other models at 400 and 550 km altitude during quiet and storm conditions. Although WAM-IPE is slightly higher than other models at 200 km altitude, this is only the case during quiet conditions; TIE-GCM has the highest density during the storm at 200 km altitude. JB2008 and TIE-GCM have similar day-to-day performance at all three altitude shells during this time period. Similarly, DTM and MSIS2.0 agree with each other at 400 and 550 km altitude, but are separated and lower than other models at 200 km. There is a predominantly positive correction applied to JB2008 in HASDM, which is solved for via assimilation of real-time satellite position data, showing that satellite data indicates higher density than JB2008 during quiet and storm conditions. HASDM and WAM-IPE appear to show post-storm overcooling (cooling to a lower level of density than the quiet conditions before the storm [35], [36], [33]. This indicates that the assimilated information from satellite orbits in HASDM shows post-storm cooling and suggests that WAM-IPE models post-storm constituent dynamics better than TIE-GCM. We note that solar activity is high enough during this time period such that TIE-GCM maximum altitude is higher than 550 km and thus does not need to be extrapolated to obtain these results. Overall, at the higher altitude of 550 km where most LEO satellites orbit, there is

a factor of 2 difference between the model with the lowest (TIEGCM and JB2008) and highest (WAM-IPE) global density outputs. Excluding WAM-IPE at this altitude shell, that difference is approximately 30%. This large discrepancy in absolute global densities is an indication of the current status thermospheric density modeling.

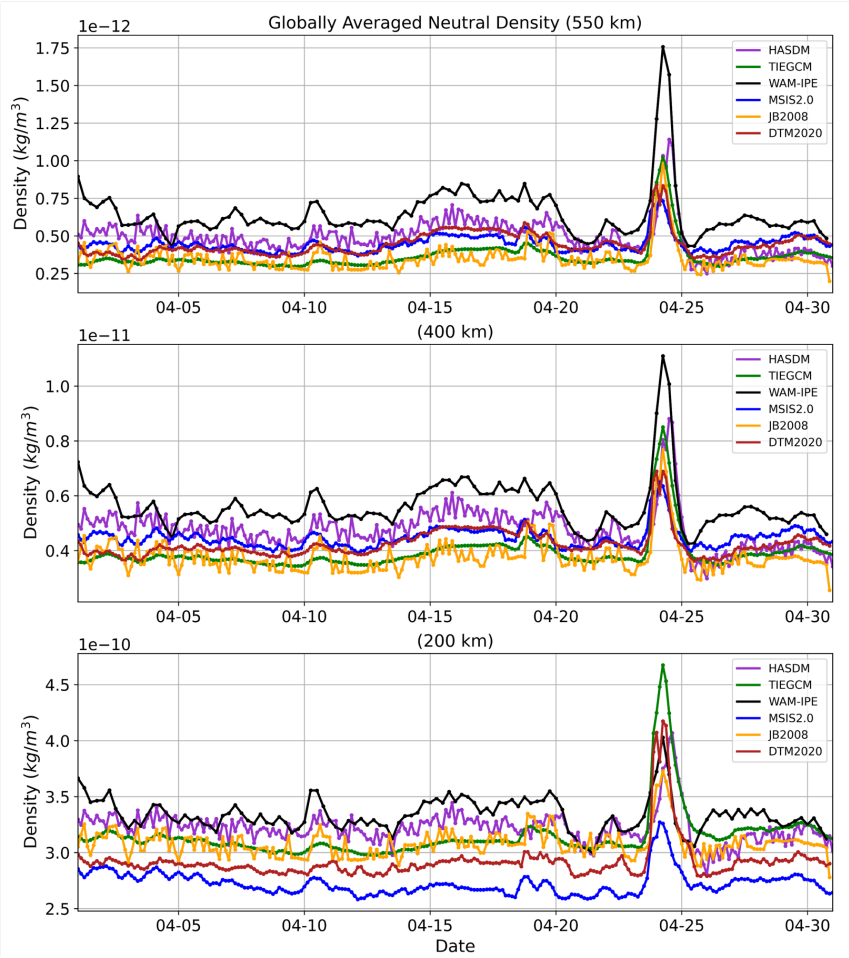

Fig. 6. Globally averaged density at altitude shells of 200, 400, and 550 km

5.2 Global Density Evaluation Metrics

Now we quantify the performance of each model's density by comparing it to HASDM density via the metrics presented in [82], [83]. These metrics include $\mu(m/o)$, $\sigma(m/o)$, and R$MSe(m/o)$, all in log space

$$\mu(m/o) = exp\left(\frac{1}{N}\sum_{i=1}^{N}\ln\frac{\rho_{m,i}}{\rho_{o,i}}\right) \tag{3}$$

$$\sigma(m/o) = \sqrt{\frac{1}{N}\sum_{i=1}^{N}\left(ln\frac{\rho_{m,i}}{\rho_{o,i}} - \ln\mu(m/o)\right)^2} \tag{4}$$

$$RMSe(m/o) = \sqrt{\frac{1}{N}\sum_{i=1}^{N}\left(ln\frac{\rho_{m,i}}{\rho_{o,i}}\right)^2}$$

(5)

where "m" is the *model* density and "o" is the *observed* density, or the closest to truth density that is available (i.e., HASDM). N is the total number of data points included in the calculation. For this work, the metrics are calculated globally for each altitude shell separately; so, N = 456, which is a data point every one hour in LST and every 10-deg in latitude (24 LSTs x 19 latitudes). The $\sigma(m/o)$ and $RMSe(m/o)$ quantities are best interpreted as percentages, using:

$$\% = 100 \times (\exp \sigma(m/o) - 1)$$

(6)

μ indicates density bias, where $\mu = 1$ is no bias between the model and HASDM. Root Mean Squared error (RMSe) is a good indicator of total model errors, and σ is an indication of the spread of the errors (i.e., variance).

The global density evaluation metrics are provided for each model throughout the month of April 2023 in Fig.7. Metrics are computed between each model (m) and HASDM (o), globally, at a 3-hour time resolution. These metrics are a representation of the model performance across the globe, as opposed to a global-average, because they are computed on a point-by-point basis using the spatial resolution of HASDM, 10-deg latitude and 1-hour Local Sidereal Time (LST) (i.e., 10-deg longitude). In other words, the metrics in Fig. 7 represent the spatial error against HASDM while using a consistent spatial resolution among all models. There are features in some of the models that are probably not represented in HASDM, because temperature corrections to the JB2008 background model in HASDM have a lower spatial resolution than 10-deg latitude, 1-hour LST. These features will manifest as "errors" even though they are actually additional signal (correct or not). The overall bias, RMSe, and variance between the models and HASDM increases as altitude increases; they are lowest at 200 km altitude (μ is closer to 1) and highest at 550 km altitude. During quiet times, WAM-IPE density has the largest positive bias ($\mu > 1$), whereas other models have lower density than HASDM, indicated by $\mu < 1$. JB2008 and TIE-GCM have similar bias at all three altitude shells; DTM and MSIS have similar bias at 400 and 550 km altitude, but differ at 200 km altitude. Each model's performance is distinct at 200 km altitude; the total global error, indicated by RMSe, is lowest for JB2008 and highest for MSIS2.0 at 200 km altitude. At higher altitudes, MSIS2.0 and DTM are the better performing models in terms of bias and RMSe, followed by TIE-GCM and JB2008, then WAM-IPE.

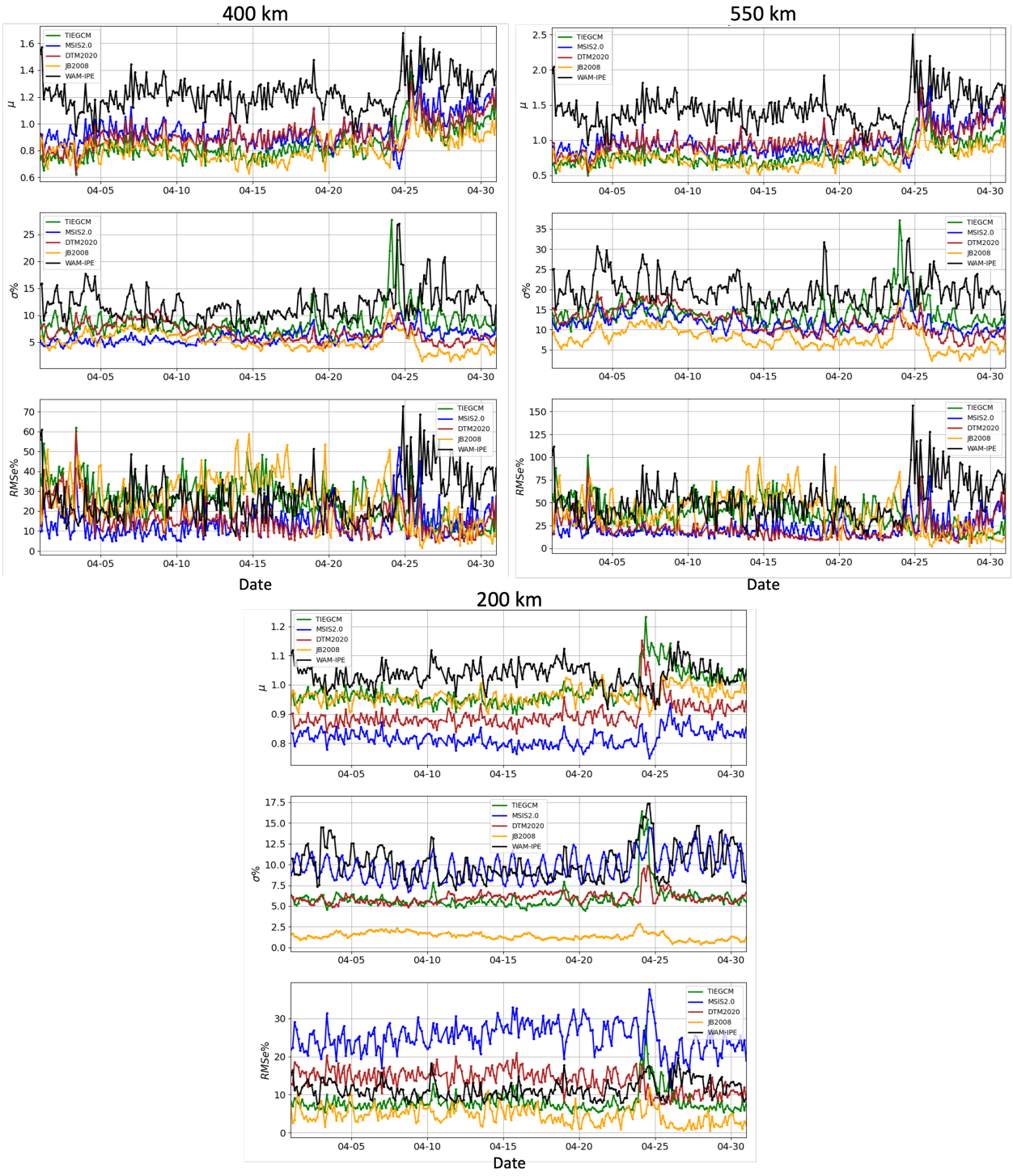

Fig. 7. Density evaluation metrics for each model with respect to HASDM at altitude shells of 200, 400, and 550 km

5.3 GRACE-FO Accelerometer-Derived Density

This section provides a comparison of each model's density to the GRACE-FO accelerometer-derived density along the orbit of GRACE-FO during the month of April 2023. The GRACE-FO mission [34], [98] consists of a pair of satellites in circular, near-polar orbits, separated by approximately 240 km along their orbital tracks. The initial altitude was about 510 km and decreased to 500 km in early 2023. With the main science objective of sensing variations in

Earth's gravitational potential, these satellites were launched in May 2018 to extend the data set of the original GRACE satellites [88], which flew 2002–2017. In addition to their primary objective, the satellites provide measurements of nonconservative forces from highly precise accelerometers that can be used to infer the neutral mass density of the thermosphere at high cadence (1 Hz) and resolution (~7.6 km along the orbit).

The density is obtained by inverting the along-track component of the aerodynamic acceleration

$$a_{aero} = \frac{1}{2}\rho\frac{C_{aero}}{m}v_{rel}^2\frac{\vec{v}_{rel}}{|\vec{v}_{rel}|} \quad (7)$$

where ρ is the neutral mass density, m is the satellite mass, $\vec{v}_{rel}$ is the satellite velocity vector relative to the atmosphere, and C_{aero} is the aerodynamic coefficient vector intrinsically scaled by the satellite's cross-section area [72]. The aerodynamic acceleration is obtained by removing the modeled radiation pressure acceleration from the measured acceleration, which is calibrated using the data from the GPS receiver. Equation 7 indicates that the scale of the density observations depends on the aerodynamic coefficient vector, which is sensitive to the underlying gas-surface interaction model (GSI) [46]. The GRACE-FO density data was produced assuming diffuse reflections with incomplete accommodation as GSI model, with an energy accommodation coefficient of 0.85. At 500 km altitude during solar minimum, this assumption may cause a scaling effect of 5% of the aerodynamic coefficient vector [5].

Fig. 8 provides the April 2023 orbit-average model and GRACE-FO accelerometer-derived densities. HASDM, DTM, and MSIS2.0 densities are most aligned with the GRACE-FO accelerometer-derived densities. WAM-IPE density is noticeably higher than other models and GRACE-FO. JB2008 and TIE-GCM have similar performance and have lower density than GRACE-FO. The GRACE-FO orbit-average accelerometer-derived densities show post-storm cooling, which is also captured by HASDM.

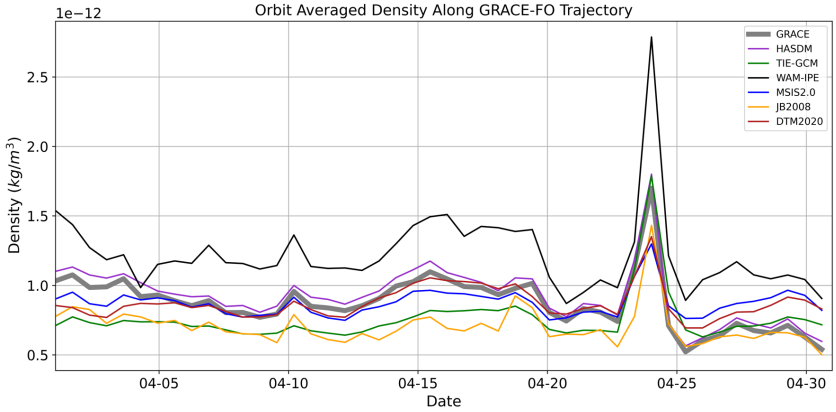

Fig. 8. Orbit-average GRACE-FO and model density

Fig. 9 provides the density along the GRACE-FO trajectory for each model (not orbit-average). We take a closer look at the quiet and storm conditions in Fig. 10, indicated by the green boxes in Fig. 9. All models have similar performance to GRACE-FO during quiet conditions. The correction between JB2008 and HASDM appears to bring the HASDM density much closer to the GRACE-FO accelerometer-derived density. GRACE-FO's polar orbit traverses through midnight and local noon, and is located at the equator during local midnight. After the storm begins on April 24th at 3 Universal Time (UT), WAM-IPE density is higher than the other models and GRACE-FO. The storm time condition density behavior is more chaotic; there are no clear density peaks as in the calm conditions case. This is because the GRACE-FO orbit has shifted and is traversing through 10 and 22 LST (morning and evening) rather than near local noon and midnight, as it was during the calm conditions. Interestingly, TIE-GCM and WAM-IPE, the physics-based models, are the only models that capture some of the high-rate variability of the GRACE-FO accelerometer-derived density, although TIE-GCM better matches the observed variability. The remaining models, all empirical-based, are only able to capture the average behavior of the true density via a relatively smooth sinusoid.

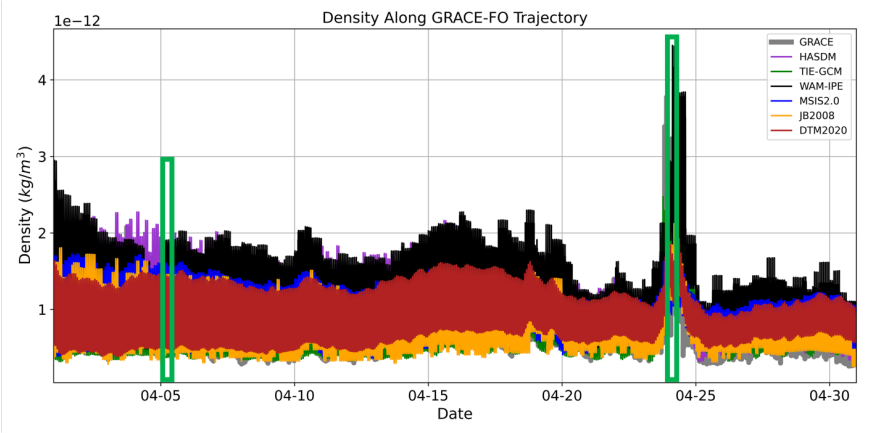

Fig. 9. Model density along the GRACE-FO trajectory for month of April 2023

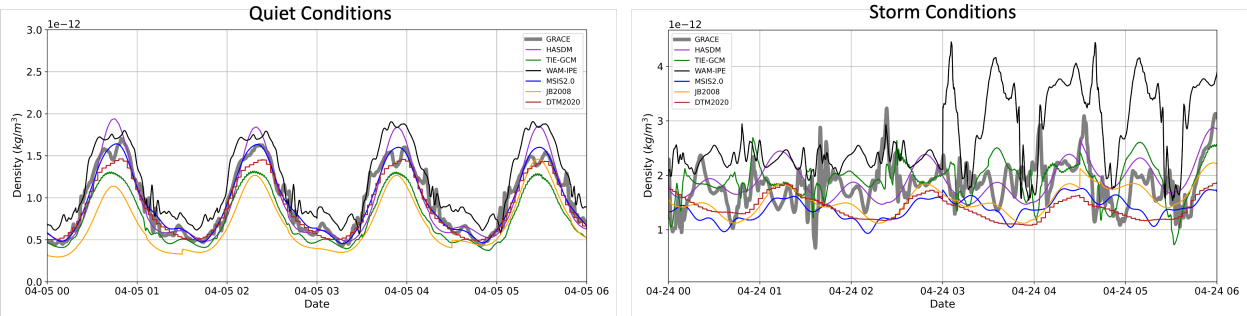

Fig. 10. Model density along the GRACE-FO trajectory during 6 hours of quiet and storm conditions

5.4 Propagation Analysis

This simulation scenario is created to study the in-track position difference between propagating a nominal CubeSat through a density field generated with each operations-ready density model and with HASDM density. For the purpose of this study, HASDM global density is considered true density. A simulated satellite in a circular orbit is propagated with each density model for one day at altitude shells of 400 and 550 km. One propagation case takes place during quiet conditions on April 5th, 2023, and another during storm conditions on April 24th 2023.

Each propagation is initialized with the same ephemeris initial conditions. The final in-track position difference between the propagation with each density model and propagation with HASDM density is computed. A smaller in-track position difference indicates a better-calibrated density model to HASDM. Each trajectory is propagated using the same dynamics; the only difference is the underlying density model.

Table 2 provides the in-track position difference between the one-day propagation with each density model and HASDM during quiet and storm conditions. Overall, the in-track position error is higher at 400 km altitude compared to 550 km due to the exponential decay of density, and therefore also drag, as a function of altitude. During quiet conditions, MSIS2.0 has the smallest in-track position error for 400 and 550 km altitude. At 400 km altitude during quiet conditions, all models have an order of magnitude higher in-track position error compared to MSIS2.0. During storm conditions, TIE-GCM has the smallest in-track position error for 400 and 550 km altitude, while WAM-IPE has the largest. At 550 km altitude during storm conditions, all models have similar performance, excluding WAM-IPE.

Table 2. One-day model density propagation in-track position error
(with respect to propagation with HASDM density)

Model / Orbit	**400 km/Quiet (km)**	**400 km/Storm (km)**	**550 km/Quiet (km)**	**550 km/Storm (km)**
DTM	-14	-29	-2	-4
JB2008	-18	-23	-2	-3
MSIS2.0	2	-20	0	-4
TIE-GCM	-16	-3	-3	-2
WAM-IPE	10	40	1	8

6. CONCLUSION

This paper provides a description of each operations-ready density model, which we define as a model that is well-documented, has verified and quantified model performance, and provides publicly available model code for implementation on a user's own system. A performance analysis of the operations-ready density models, with the addition of HASDM and WAM-IPE, is presented. This analysis is meant to provide an example of model performance over a limited time period rather than being a comprehensive evaluation of each model. The global mean density plots and comparison to GRACE-FO accelerometer-derived density provide an evaluation of each density model's performance independent of HASDM. Whereas, the density evaluation metrics and propagation analysis are computed with respect to HASDM because it is the closest to global true density that is available.

The global mean density plots show that WAM-IPE has distinctly higher density at 200, 400, and 550 km altitude shells throughout the month of April 2023. JB2008 and TIE-GCM have similar global mean densities, as do DTM and MSIS2.0. Global density evaluation metrics with respect to HASDM showed that WAM-IPE has a distinctly higher bias than other models, which aligns with the findings in the global mean density plots. JB2008 and TIE-GCM have similar bias, as do DTM and MSIS2.0 at 400 and 550 km altitude. At 200 km altitude, MSIS2.0 has a distinctly higher RMSe than other models. At 550 km altitude, MSIS2.0 and DTM are the better performing models in terms of bias and RMSe, followed by TIE-GCM and JB2008, then WAM-IPE. Orbit-averaged HASDM, DTM, and MSIS2.0 align best with GRACE-FO accelerometer-derived density. The physics-based models, TIE-GCM and WAM-IPE, capture some of the local variability of the GRACE-FO density, while the empirical-based models are only able to capture the average behavior of the GRACE-FO density via a smooth sinusoid during disturbed conditions in the morning and night. JB2008 tends to model lower densities compared to GRACE-FO and most other models throughout the analyses; this is likely due to not enough thermosphere heating input to the model via model driver S10. An updated S10 index is expected early 2024 that will improve thermosphere heating in JB2008. Lastly, a propagation analysis is presented in which a nominal CubeSat is propagated with each model and compared to the HASDM propagation. MSIS2.0 has the smallest one-day in-track propagation error during quiet conditions and TIE-GCM has the smallest during storm conditions.

Overall, the analysis shows that most of the operations-ready density models (DTM2020, JB2008, MSIS2.0, TIE-GCM) would be a viable option for satellite operations. A more comprehensive analysis is required to understand performance differences under the full range of solar and geomagnetic conditions.

For additional model comparisons, we recommend the NASA CCMC Comprehensive Assessment of Models and Events based on Library tools (CAMEL) thermosphere neutral density score card. Although currently under development, it will soon provide comprehensive model assessments of all operations-ready density models (plus a few more) during several historical storm periods [47].

7. REFERENCES

[1] Ansys Orbit Determination Tool Kit: https://www.ansys.com/products/missions/ansys-odtk

[2] Barlier, F., Berger, C., Falin, J.L., Kockarts, G., Thuillier, G. 1978. A thermospheric model based on satellite drag data, Ann. Geophys, 34, 9-24.

[3] Bernese GNSS Software: http://www.bernese.unibe.ch

[4] Bernstein, V., Pilinski, M., Knipp, D., 2021. Drag coefficient constraints for space weather observations in the upper thermosphere. J. Spacecraft Rock. 57 (6), 1246–1263. https://doi.org/10.1002/essoar.10508667.1

[5] Bernstein, V., Pilinski, M. 2022. Drag coefficient constraints for space weather observations in the upper thermosphere. Space Weather 20: e2021SW002977. https://doi.org/10.1029/2021SW002977

[6] Bertiger, W. et al. 2020. GipsyX/RTGx, a new tool set for space geodetic operations and research, Advances in Space Research, Volume 66, Issue 3, Pages 469-489, ISSN 0273-1177, https://doi.org/10.1016/j.asr.2020.04.015.
[7] Bowman, B., Storz, M.F. 2002. Time series analysis of HASDM thermospheric temperature and density corrections. AIAA/AAS Astrodynamics Specialist Conference.
[8] Bowman, B., Storz, M.F. 2003. High accuracy satellite drag model (HASDM) review. Advances in the Astronautical Sciences, 116:1943–1952.
[9] Bowman, B.R., Tobiska, W.K., Marcos, F.A., Huang, C.Y., Lin, C.S., Burke, W.J. 2008. A New Empirical Thermospheric Density Model JB2008 Using New Solar and Geomagnetic Indices, AIAA/AAS Astrodynamics Specialist Conference, AIAA 2008-6438.
[10] Bruinsma, S.L., Doornbos, E., Bowman, B.R. 2014. Validation of GOCE densities and thermosphere model evaluation, Adv. Space Res., 54, 576-585, doi:10.1016/j.asr.2014.04.008.
[11] Bruinsma, S.L. 2015. The DTM-2013 thermosphere model, J. Space Weather Space Clim., DOI: https://doi.org/10.1051/swsc/2015001
[12] Bruinsma, S., Sutton, E., Solomon, S.C., Fuller-Rowell, T., Fedrizzi, M. 2018. Space Weather Modeling Capabilities Assessment: Neutral Density and Orbit Determination at LEO, Space Weather, doi.org/10.1029/2018SW002027
[13] Bruinsma, S., Boniface, C. 2021. The DTM2020 thermosphere models, J. Space Weather Space Clim., https:/doi.org/10.1051/swsc/2021032
[14] Bruinsma, S., Boniface, C., Sutton, E., Fedrizzi, M. 2021. Thermosphere Modeling Capabilities Assessment: Geomagnetic Storms. Journal of Space Weather and Space Climate. 11. 10.1051/swsc/2021002.
[15] CelesTrak Space Weather Data: https://celestrak.org/SpaceData/SpaceWx-format.php
[16] CLS F30 Nowcast and Forecast: https://spaceweather.cls.fr/services/radioflux/
[17] Dickinson, R.E., Ridley, E.C., Roble, R.G. 1981. A three-dimensional general circulation model of the thermosphere, J. Geophys. Res., 86, 1499-1512.
[18] Dickinson, R.E., Ridley, E.C., Roble, R.G. 1984. Thermospheric general circulation with coupled dynamics and composition, J. Atmos. Sci., 41, 205-219.
[19] Doornbos, E., Bruinsma, S., Fritsche., B, Koppenwallner, G., Visser, P., Van Den IJssel, J., de Teixeira de Encarnação, J. 2014. ESA contract 4000102847/NL/EL, GOCE+ Theme 3: Air density and wind retrieval using GOCE data – Final Report, TU Delft.
[20] Doornbos E. 2011. Thermospheric density and wind determination from satellite dynamics, Ph.D. Dissertation, 188 pp., University of Delft, available at http://repository.tudelft.nl/.
[21] Emmert, J.T. et al. 2020. NRLMSIS 2.0: A whole-atmosphere empirical model of temperature and neutral species densities, Earth and Space Science, https://doi.org/10.1029/2020EA001321.
[22] Emmert, J.T. 2015. Altitude and solar activity dependence of 1967–2005 thermospheric density trends derived from orbital drag, J. Geophys. Res. Space Physics, 120, 2940–2950, doi:10.1002/ 2015JA021047.
[23] Fang, T.W., Kubaryk, A., Goldstein, D., Li, Z., Fuller-Rowell, T., Millward, G., Singer, H., Steenburgh, R., Westerman, S., Babcock, E. 2022. Space Weather Environment During the SpaceX Starlink Satellite Loss in February 2022. Space Weather. 20. 10.1029/2022SW003193.
[24] Fitzgerald, R.M., Cahoy, K.L. 2019. Localized in-situ density measurement in low earth orbit via drag torque estimation. Journal of Spacecraft and Rockets, 56(5).
[25] GFZ German Centre for Geosciences: https://kp.gfz-potsdam.de/en/
[26] GFZ German Centre for Geosciences Geomagnetic Indices: https://www.gfz-potsdam.de/en/section/geomagnetism/data-products-services/geomagnetic-kp-index).
[27] Hagan, M.E., Roble, R.G., Hackney, J. 2001. Migrating thermospheric tides. J Geophys Res 106: 12739–12752. https://doi.org/10.1029/ 2000JA000344.
[28] Heelis, R.A., Lowell, J.K., Spiro, R.W. 1982. A model of the high-latitude ionosphere convection pattern. J Geophys Res 87: 6339. https://doi.org/10.1029/JA087iA08p06339.
[29] International Organization for Standardization. 2022. Space environment (natural and artificial) — Earth's atmosphere from ground level upward. (ISO Standard No. 14222:2022). https://www.iso.org/standard/77492.html
[30] Jacchia, L.G. 1970. 'New Static Models of the Thermosphere and Exosphere with Empirical Temperature Profiles', Smithsonian Institution Astrophysical Observatory, SAO Special Report No. 313, Cambridge, Mass.
[31] Knipp, D.J., Tobiska, W.K., Emery, B.A. 2004. Direct and indirect thermosphere heating sources for solar cycle 21-23. Solar Physics, 224:495–505. https://doi.org/10.1007/s11207-005-6393-4
[32] Knipp, D. J., 2011. Understanding Space Weather and the Physics Behind It, McGraw Hill, now in 2nd Edition as e-book by Space Technology Series: http://store.spacetechnologyseries.com/ebooks/17-understanding-space-weater-and-the-physics-behind-it.html

[33] Knipp, D.J., Pette, D.V., Kilcommons, L.M., Isaacs, T.L., Cruz, A.A., Mlynczak, M.G., Hunt, L.A., and Lin, C.Y. 2017. Thermospheric nitric oxide response to shock-led storms, Space Weather, 15, 325–342, doi:10.1002/2016SW001567.
[34] Kornfeld, R.P., Arnold, B.W., Gross, M.A., Dahya, N.T., Klipstein, W.M., Gath, P.F., Bettadpur, S. 2019. GRACE-FO: The Gravity Recovery and Climate Experiment Follow-On Mission. Journal of Spacecraft and Rockets, 56(3), 931–951. https://doi.org/10.2514/1.A34326

[35] Lei, J., Thayer, J.P., Lu, G., Burns, A.G., Wang, W., Sutton, E.K., Emery, B.A. 2011. Rapid recovery of thermosphere density during the October 2003 geomagnetic storms, J. Geophys. Res., 116, A03306, doi:10.1029/2010JA016164.
[36] Lei, J., Burns, A.G., Thayer, J.P., Wang, W., Mlynczak, M.G., Hunt, L.A., Dou, X., Sutton, E. 2012. Overcooling in the upper thermosphere during the recovery phase of the 2003 October storms, J. Geophys. Res., 117, A03314, doi:10.1029/2011JA016994.
[37] Licata, R.J., Tobiska, W.K., Mehta, P.M. 2020. Benchmarking forecasting models for space weather drivers. *Space Weather*, *18*, e2020SW002496. https://doi.org/ 10.1029/2020SW002496
[38] Liying, Q., Burns, A., Emery, B., Foster, B., Lu, G., Maute, A., Richmond, A., Roble, R., Solomon, S., Wang. 2014. The NCAR TIE-GCM: A community model of the coupled thermosphere/ionosphere system. In Book: Modeling the Ionosphere-Thermosphere System, edited by J. D. Huba, pages 73–83. Geophysical Mono- graph Series, vol. 201.
[39] Marcos, F., Bowman, B., Sheehan, R. 2006. Accuracy of Earth's Thermospheric Neutral Density Models. 10.2514/6.2006-6167.
[40] March, G., Doornbos, E., Visser, P. 2019. High-fidelity geometry models for improving the consistency of CHAMP, GRACE, GOCE and Swarm thermospheric density data sets, Adv. Space Res., 63, 1, 213-238, https://doi.org/10.1016/j.asr.2018.07.009
[41] March, G., van den Ijssel, J., Siemes, C., Visser, P., Doornbos, E., Pilinski, M. 2019. Gas-surface interactions modelling influence on satellite aerodynamics and thermosphere mass density, J. Space Weather Space Climate, 11, 54, doi:10.1051/swsc/2021035
[42] Maruyama, N. et al. 2016. 'A new source of the midlatitude ionospheric peak density structure revealed by a new Ionosphere-Plasmasphere model', Geophysical Research Letters, 43(6), pp. 2429–2435. Available at: https://doi.org/10.1002/2015GL067312.
[43] MATLAB Jacchia-Bowman Atmospheric Density Model: https://www.mathworks.com/matlabcentral/fileexchange/56163-jacchia-bowman-atmospheric-density-model
[44] Mehta, P.M., Walker, A., Lawrence, E., Linares, R., Higdon, D., Koller, J. 2014. Modeling Satellite Drag Coefficients with Response Surfaces, Adv. Space Res., 54, 8, pp. 1590-1607, https://doi.org/10.1016/j.asr.2014.06.033
[45] Mehta, R., Linares, R., Sutton, E.K. 2019. Data-driven inference of thermosphere composition during solar minimum conditions. Space Weather, 17:1364–1379.
[46] Mehta, P.M., Paul, S.N., Crisp, N.H., Sheridan, P.L., Siemes, C., March, G., Bruinsma, S. 2022. Satellite drag coefficient modeling for thermosphere science and mission operations, Adv. Space Res., https://doi.org/10.1016/j.asr.2022.05.064
[47] NASA CCMC CAMEL Neutral Density: https://webserver1.ccmc.gsfc.nasa.gov/camel/NeutralDensity/
[48] NASA CCMC WAM-IPE Model: https://ccmc.gsfc.nasa.gov/news/wamipe-update/
[49] NASA General Mission Analysis Tool: https://software.nasa.gov/software/GSC-17177-1
[50] NASA Goddard GEODYN: https://space-geodesy.nasa.gov/techniques/tools/GEODYN/GEODYN.html
[51] NASA JPL MONTE: https://montepy.jpl.nasa.gov
[52] National Science and Technology Council, 2015, National Space Weather Action Plan, Washington, DC, October, https://www.hsdl.org/?view&did=789864. Space Weather Advisory Group (2023), Findings and Recommendations to Successfully Implement PROSWIFT and Transform the National Space Weather Enterprise, April 17, 2023
[53] NCAR High Altitude Observatory TIE-GCM: https://www.hao.ucar.edu/modeling/tgcm/tie.php
[54] NOAA NCEI Geomagnetic Indices: https://www.ngdc.noaa.gov/stp/geomag/kp_ap.html
[55] NOAA SWPC 3-Day Geomagnetic Forecast: https://www.swpc.noaa.gov/products/3-day-geomagnetic-forecast
[56] NOAA SWPC 45-Day Ap and F10.7 Forecast:
[57] https://www.swpc.noaa.gov/products/usaf-45-day-ap-and-f107cm-flux-forecast
[58] NOAA SWPC Solar Cycle Progression. https://www.swpc.noaa.gov/products/solar-cycle-progression
[59] NOAA SWPC WAM-IPE: https://registry.opendata.aws/noaa-nws-wam-ipe/
[60] Orekit Astrodynamics Toolkit DTM2000: https://www.orekit.org/static/apidocs/org/orekit/models/earth/atmosphere/DTM2000.html
[61] Orekit Astrodynamics Toolkit JB2008: https://www.orekit.org/static/apidocs/org/orekit/models/earth/atmosphere/JB2008.html

[62] Orekit Astrodynamics Toolkit MSIS: https://www.orekit.org/static/apidocs/org/orekit/models/earth/atmosphere/NRLMSISE00.html
[63] Pilinski, M.D., Argrow, B.M., Palo, S.E. 2013. Semi-empirical satellite accommodation model for spherical and randomly tumbling objects, J. Spacecraft and Rockets, 50, pp. 556-571, https://doi.org/10.2514/1.A32348
[64] Pilinski, M.D. 2016. "Physics-based assimilative atmospheric modeling for satellite drag specification and forecasts". Advances in the Astronautical Sciences(0065-3438), 156 , p. 4405.
[65] Qian, L., Burns, A.G., Emery, B.A., Foster, B., Lu, G., Maute, A., Richmond, A.D., Roble, R.G., Solomon, S.C., Wangm, W. 2014. The NCAR TIE-GCM: A community model of the coupled thermosphere/ionosphere system, in Modeling the Ionosphere-Thermosphere System, AGU Geophysical Monograph Series.
[66] Ray, V., Berger, T. E., Waldron, Z.C., Sutton, E.K., Lucas, G., Knipp D.J., Thayer, J.P., Hesar, S.G., Scheeres, D.J. 2022. The impact of space weather on very low Earth orbit (VLEO) satellites, Advanced Maui Optical and Space Surveillance Technologies Conference (AMOS) 2022, https://amostech.com/TechnicalPapers/2022/Atmospherics_Space-Weather/Ray.pdf
[67] Richards, P.G. et al. 1994. 'Ionospheric effects of the March 1990 Magnetic Storm: Comparison of theory and measurement', Journal of Geophysical Research, 99(A12), p. 23359. Available at: https://doi.org/10.1029/94JA02343.
[68] Richards, P.G., Fennelly, J.A., Torr, D.G. 1994. 'EUVAC: A solar EUV Flux Model for aeronomic calculations', Journal of Geophysical Research, 99(A5), p. 8981. Available at: https://doi.org/10.1029/94JA00518.
[69] Richmond, A.D., Ridley, E.C. and Roble, R.G. 1992. 'A thermosphere/ionosphere general circulation model with coupled electrodynamics', Geophysical Research Letters, 19(6), pp. 601–604. Available at: https://doi.org/10.1029/92GL00401.
[70] Roble, R.G., Dickinson, R.E., Ridley, E.C. 1982. Global circulation and temperature structure of the thermosphere with high-latitude plasma convection, J. Geophys, Res., 87, 1599-1614.
[71] Sentman, L.H. 1961. Comparison of the exact and approximate methods for predicting free molecule aerodynamic coefficients, ARS J., 31, 1576–1579.
[72] Siemes, C., Borries, C., Bruinsma, S., Fernandez-Gomez, I., Hładczuk, N., van den IJssel, J., Kodikara, T., Vielberg, K., Visser, P. 2023. New thermosphere neutral mass density and crosswind datasets from CHAMP, GRACE, and GRACE-FO. Journal of Space Weather and Space Climate, 13, 16. https://doi.org/10.1051/swsc/2023014
[73] Space Environment Technologies HASDM Density Database: https://spacewx.com/hasdm
[74] Space Environment Technologies JB2008: https://sol.spacenvironment.net/JB2008/
[75] Space Weather Advisory Group, Findings and Recommendations to Successfully Implement PROSWIFT and Transform the National Space Weather Enterprise, 2023, https://www.weather.gov/media/nws/REPORT-Findings-and-Recommendations-04202023.pdf
[76] Space Weather Prediction Center. Station K and A indices. www.swpc.noaa.gov/products/ station-k-and-indices, 2021. November 18, 2021.
[77] Storz, M.F., Bowman, B.R., Branson, M.J.I., Casali, S.J., Tobiska, W.K. 2005. High accuracy satellite drag model (HASDM), Adv. Space Res., 36, 2497–2505, doi:10.1016/j.asr.2004.02.020.
[78] Sugiura, M., Kamei T. 1991. Equatorial Dst Index 1957–1986, IAGA Bull, vol. 40, ISGI Pub. Office, Saint-Maur-des-Fossess, France. https://isgi.unistra.fr/Documents/References/Sugiura_Kamei_IAGAB_1991.pdf
[79] Sun, Y. et al. 2015. 'Field-aligned neutral wind bias correction scheme for global ionospheric modeling at midlatitudes by assimilating FORMOSAT-3/COSMIC H M F 2 data under geomagnetically quiet conditions', Journal of Geophysical Research: Space Physics, 120(4), pp. 3130–3149. Available at: https://doi.org/10.1002/2014JA020768.
[80] Sutton, E. 2009. Normalized force coefficients for satellites with elongated shapes. Journal of Spacecraft and Rockets, 46(1):112–116.
[81] Sutton, E., Cable, S., Lin, C., Qian, L., Weimer, D.R. 2012. Thermospheric basis functions for improved dynamic calibration of semi-empirical models. Space Weather, 10.
[82] Sutton, E. K. 2018. A new method of physics-based data assimilation for the quiet and disturbed thermosphere. Space Weather, 16, 736–753. https://doi.org/10.1002/2017SW001785.
[83] Sutton, E., Thayer, J., Pilinski, M., Mutschler, S., Berger, T., Nguyen, V., Masters, D. 2021. Toward accurate physics-based specifications of neutral density using GNSS-enabled small satellites. Space Weather, 19.
[84] SWAMI Drag Temperature Model 2020: https://swami-h2020-eu.github.io/mcm/dtm2020.html
[85] SWx TREC Coefficient of Drag Model: https://swx-trec.com/vector/
[86] SWx TREC Python MSIS Wrapper: https://pypi.org/project/pymsis/
[87] SWx TREC TIE-GCM via Docker: https://gallery.ecr.aws/swx-trec/tiegcm

[88] Tapley, B.D., Bettadpur, S., Watkins, M., Reigber, C. 2004. The gravity recovery and climate experiment: Mission overview and early results: GRACE MISSION OVERVIEW AND EARLY RESULTS. Geophysical Research Letters, 31(9), n/a-n/a. https://doi.org/10.1029/2004GL019920
[89] Thayer, J., Tobiska, W.K., Pilinski, M.D., Sutton, E.K. 2021. Remaining issues in upper atmosphere satellite drag, *Space Physics and Aeronomy, Volume 5, Space Weather Effects and Applications*, eds. Coster A.J., Erickson, P.J., Lanzerotti, L.J., Zhang, Y., Paxton, L.J., AGU Books, p. 111, ISBN: 978-1-119-50757-4.
[90] Tobiska, W.K., Bouwer, S.D., Bowman, B.R. 2008. The development of new solar indices for use in thermospheric density modeling, *JASTP,* 70, 803-819.
[91] Tobiska, W.K., Bowman, B., Bouwer, D., Cruz, A., Wahl, K., Pilinski, M., Mehta, P., Licata, R. 2021. The SET HASDM density database. Space Weather. 19. 10.1029/2020SW002682.
[92] U.S. Naval Research Laboratory MSIS2.0: https://map.nrl.navy.mil/map/pub/nrl/NRLMSIS/NRLMSIS2.0/
[93] Vallado. 2013. Fundamentals of Astrodynamics and Applications. Space Technology Library.
[94] Van den Ijssel, J., Doornbos, E., Iorfida, E., March, G., Siemes, C., Montenbruck, O. 2020. Thermosphere densities derived from Swarm GPS observations, Advances in Space Research, vol. 65, 7, doi.org/10.1016/j.asr.2020.01.004.
[95] Viereck, R.A., Puga, L.C. 1999. The NOAA Mg II core-to-wing solar index: Construction of a 20-year time series of chromospheric variability from multiple satellites. Journal of Geophysical Research. vol. 104, no. A5, pp. 9995–10006, 1999. doi:10.1029/1998JA900163.
[96] Weimer, D.R. 2005. Improved ionospheric electrodynamic models and application to calculating Joule heating rates. J Geophys Res 110: A05306. https://doi.org/10.1029/2004JA010884.
[97] World Data Center for Geomagnetism, Kyoto, Nose, M., Iyemori, T., Sugiura, M., Kamei, T. 2015. Geomagnetic Dst index, doi:10.17593/14515-74000
[98] Wen, H.Y., Kruizinga, G., Paik, M., Landerer, F., Bertiger, W., Sakumura, C., Bandikova, T., Mccullough, C. 2019. Gravity recovery and climate experiment follow-on (GRACE-FO) level-1 data product user handbook, Technical report JPL D-56935 (URS270772). NASA Jet Propulsion Laboratory, California Institute of Technology.
[99] WDC Real-time Dst Index: https://wdc.kugi.kyoto-u.ac.jp/dst_realtime/index.html